Available online at www.sciencedirect.com
ScienceDirect
Journal of Nuclear Materials 367–370 (2007) 527–538
journal of nuclear materials
www.elsevier.com/locate/jnucmat

Plastic flow properties and fracture toughness characterization of unirradiated and irradiated tempered martensitic steels

P. Spätig [a,*], R. Bonadé [a], G.R. Odette [b], J.W. Rensman [c], E.N. Campitelli [a], P. Mueller [a]

[a] *Fusion Technology-Materials, CRPP/EPFL, Association EURATOM-Confédération Suisse, 5232 Villigen PSI, Switzerland*
[b] *Department of Mechanical and Environmental Engineering, University of California, Santa Barbara, CA 93106-5070, USA*
[c] *NRG, P.O. Box 25, 1755 ZG Petten, The Netherlands*

Abstract

We investigate the plastic flow properties at low and high temperature of the tempered martensitic steel Eurofer97. We show that below room temperature, where the Peierls friction on the screw dislocation is active, it is necessary to modify the usual Taylor's equation between the flow stress and the square root of the dislocation density and to include explicitly the Peierls friction stress in the equation. Then, we compare the fracture properties of the Eurofer97 with those of the F82H steel. A clear difference of the fracture toughness–temperature behavior was found in the low transition region. The results indicate a sharper transition for Eurofer97 than for the F82H. Finally, the shift of the median toughness–temperature curve of the F82H steel was determined after two neutron irradiations performed in the High Flux Reactor in Petten.

1. Introduction

Advanced tempered martensitic steels are leading candidate materials for fusion rector structural components due to their resistance to void swelling and good balance of physical and mechanical properties. Since the materials surrounding the burning plasma in a future fusion reactor will be highly irradiated by energetic neutrons and other types of radiation, a degradation of their overall mechanical properties induced by the radiation environment will occur. The degradation of the fracture toughness properties is reflected in an upward shift of the transition temperature between the brittle and ductile modes of fracture (embrittlement) as well as in a decrease of the fracture toughness in the ductile mode. One very efficient way to characterize the embrittlement is to make use of the master curve–temperature (MC) shifts method [1,2]. Basically, the MC method assumes an invariant median toughness–temperature curve that can be indexed on an absolute temperature by T_0 at a reference

* Corresponding author. Tel.: +41 56 310 29 34; fax: +41 56 310 45 29.
E-mail address: philippe.spatig@psi.ch (P. Spätig).

0022-3115/$ - see front matter © 2007 Elsevier B.V. All rights reserved.
doi:10.1016/j.jnucmat.2007.03.038

toughness of 100 MPa $m^{1/2}$. The ASTM E1921-03 standard describes the procedure to determine T_0 with a relatively small number of specimens. Since very small specimens are foreseen for future fusion irradiation facilities, efforts are being made to develop physically-based models to assess size effects on fracture toughness. These models are based upon a local approach of quasi-cleavage where a critical state of stress/strain fields at the crack tip has to be reached to trigger cleavage [3]. These fields are calculated by finite element simulations for which the constitutive behavior of the material has to be well characterized.

In this paper, we study the post-yield behavior of the tempered martensitic steel Eurofer97 steel over a large temperature range. We compare the fracture properties in the lower transition region of the Eurofer97 with those of the F82H steel and we determine the shift of the master curve after two neutron irradiations of the F82H steel.

2. Experimental

2.1. Materials

The first alloy in this study is the reduced activation Eurofer97 steel, heat E83697, 25 mm thick, produced by Böhler AG. This steel contains 8.90 wt% Cr, 0.12 wt% C, 0.46 wt% Mn, 1.07 wt% W, 0.2 wt% V, 0.15 wt% Ta, and Fe for the balance. The steel was heat-treated by normalizing at 1253 K for 0.5 h and tempering at 1033 K for 1.5 h. The second investigated alloy is the F82H steel, produced by NKK Corporation under the sponsorship of JAERI [4]. The composition is: 7.65 wt% Cr, 2.0 wt% W, 0.1 wt% C, 0.18 wt%V, 0.04 wt% Ta, and Fe for the balance. The heat treatment was 0.5 h at 1313 K for normalization and 2 h at 1013 K for tempering. These steels were fully martensitic after quenching.

2.2. Mechanical testing

Tensile tests were carried out with a Schenck RMC100 electro-mechanical testing machine. Standard DIN round specimens were used with 3 mm diameter and 18 mm gauge length. The tests were performed at several temperatures from 77 K up to 723 K. A temperature chamber was mounted around the load train. Temperature control was provided by a PID controller along with a regulated N_2 gas flow. The tests were performed at two slightly different nominal strain-rates of $9.3 \times 10^{-5}\ s^{-1}$ and $5 \times 10^{-4}\ s^{-1}$. The stresses and strains reported hereafter are the true stress and true strain. The experimental data were machine-compliance corrected except at room temperature where a clip-gage was used.

In order to investigate the strain-hardening behavior, the flow stress was decomposed into two components, namely, the yield stress $\sigma_{0.2}$, defined at 0.002 plastic strain, and the so-called plastic stress σ_{d-d} defined as $\sigma_{d-d} = \sigma - \sigma_{0.2}$. The subscript 'd–d' indicates that this component mainly stems from dislocation–dislocation interactions. In the following plots of σ_{d-d} versus ε_p, the origin of the plastic strain axis was chosen at the yield stress so that ε_p is defined as

$$\varepsilon_p = \varepsilon - \frac{\sigma(\varepsilon)}{E(T)} - 0.002, \tag{1}$$

where $\sigma(\varepsilon)$ is the true flow stress, ε is the total true strain and $E(T)$ is Young's modulus, which slightly depends on temperature. The temperature dependence of E was similar to that of the F82H steel and calculated from [5]. Finally, the strain-hardening θ_p is defined as

$$\theta_p = \frac{d\sigma_{d-d}}{d\varepsilon_p}. \tag{2}$$

The static fracture tests were performed on fatigue pre-cracked compact tension specimens, $C(T)$, with crack length a to specimen width W ratios of $a/W \approx 0.5$ and a specimen thickness (B) to width ratio of $B/W = 0.5$. Two specimen sizes were used having a thickness of either $B = 9$ mm or 4.5 mm, which are here referred as to 0.35T $C(T)$ or 0.18T $C(T)$, respectively. The fracture toughness of the Eurofer97 steel was characterized with 0.35T $C(T)$ specimens while that of the F82H steel was studied with both 0.18T $C(T)$ and 0.35T $C(T)$ specimens. Test procedures were based on ASTM practices to determine the elastic toughness K_{Ic} (ASTM E399) or the critical J-integral J_c at the onset of cleavage (ASTM E1921), from which an equivalent toughness K_{Jc} can be calculated as

$$K_{Jc} = \sqrt{\frac{J_c E}{(1-\upsilon^2)}} = \sqrt{J_c E'}, \tag{3}$$

where J_c is the elastic–plastic cleavage initiation toughness and E' is the plane strain Young's modulus.

2.3. Irradiations

The effects of neutron irradiation on fracture toughness in the low transition region of the F82H steel have been investigated using 0.18T $C(T)$ and 0.35T $C(T)$ specimens fatigue pre-cracked up to $a/W \approx 0.5$. Two different irradiations were performed in the High Flux Reactor in Petten. The conditions of the first one, SIWAS-09, were about 2.2 ± 0.3 dpa and the specimens were in contact with the reactor water coolant at a temperature of about 333 K. The second irradiation, SUMO-07, was carried out up to a similar dose of about 2.1 ± 0.1 dpa and the specimens were at a higher temperature of 573 K. The SUMO capsule was sodium-filled.

3. Plastic flow modeling of the Eurofer97

3.1. Tensile behavior

The Eurofer97 tensile properties over the temperature range 77 K up to 723 K are presented in this section. First, the yield stress, $\sigma_{0.2}$ defined at 0.2% of plastic strain, is plotted against the absolute temperature in Fig. 1. A strong increase of $\sigma_{0.2}$ with decreasing temperature is observed below about 200 K while the temperature dependence becomes much weaker above this temperature. Such a dependence is characteristic of the bcc metals and alloys and is related to the strong thermally activated lattice friction of Peierls type on the screw dislocation segments controlling the plastic flow at low temperatures [6,7]. In Fig. 2, the tensile curves obtained at the nominal strain-rates of $9.3 \times 10^{-5}\ s^{-1}$ are presented. It can be seen that all the curves have a parabolic shape. However, we point out that at 77 K an initial stage of plastic deformation at almost constant stress is observed. Note that the curves are plotted up to the true uniform strain, ε_u, at which necking starts. The true uniform strain, ε_u, is related to the uniform engineering strain, e_u, through the relation $\varepsilon_u = \ln(1 + e_u)$. Beyond ε_u, the deformation becomes localized leading to the formation of the neck. The condition at which necking begins is defined by the Considère's criterion, $\theta = \sigma$, where θ is the strain-hardening rate, defined as $d\sigma/d\varepsilon$, and σ is the true stress. This criterion is actually valid for strain-rate insensitive material. In Fig. 2, it is observed that, over the temperature range investigated, the maximum true uniform strain occurs at about 143 K. If the strain-hardening were

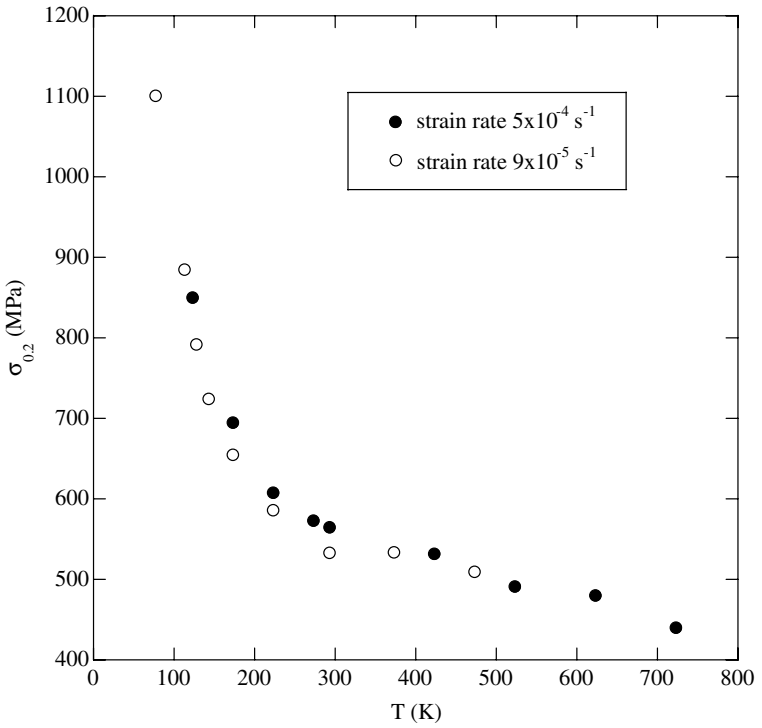

Fig. 1. Temperature dependence of the yield stress, $\sigma_{0.2}$ – Eurofer97 steel.

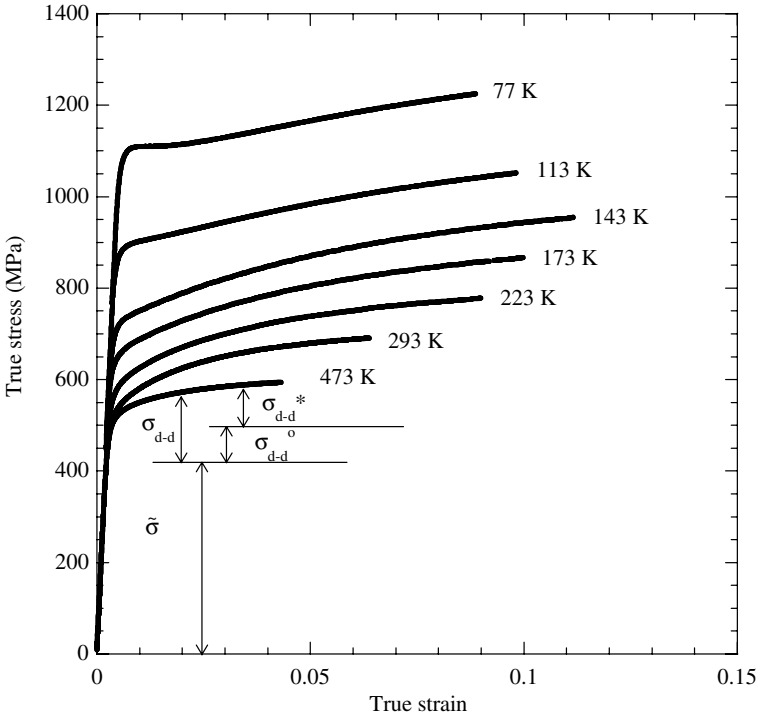

Fig. 2. Eurofer97 tensile curves at different temperatures at the nominal strain-rate of $9.3 \times 10^{-5}\ s^{-1}$. The schematic decomposition of the flow stress is also indicated.

completely athermal, or in other words, if the shape of the tensile curves were temperature independent, the true uniform strain should decrease with temperature since any increase of the flow stress with decreasing temperature would lead to the necking condition ($\sigma = \theta$) at lower strain. However, from 473 K down to 143 K, the inverse behavior is actually observed; an increase of the true uniform strain by decreasing temperature. This clearly indicates that, even if the shapes of the tensile curves at different temperatures are similar to one another, there are some subtle differences in the strain-hardening behavior that have to be identified by analyzing the post-yield behavior. This is the objective of the next two sections.

3.2. Strain-hardening behavior above room temperature

In order to model the stress dependence of the plastic strain-hardening $\theta_p(\sigma_{d-d})$, we used the simplified phenomenological description of strain-hardening based on the *one structural parameter model* initially proposed by Kocks [8] and later extended by Estrin and Mecking [9]. The structural parameter of the model is the total dislocation density, ρ, irrespective of the dislocation arrangement. First, we decompose the flow stress into two components as indicated in Fig. 2. The first component, $\tilde{\sigma}$, accounts for the grain boundaries, carbides, oxides, precipitates, solid solutions, etc. The second one, σ_{d-d}, is the contribution arising from dislocation–dislocation interactions

$$\sigma = \tilde{\sigma} + \sigma_{d-d}(\varepsilon_p). \tag{4}$$

In many investigations, σ_{d-d} was shown to be proportional to $\rho^{1/2}$ [10] where ρ is the total dislocation density and is written as

$$\begin{aligned}\sigma_{d-d}(\varepsilon_p) &= M\alpha\mu b\sqrt{\rho(\varepsilon_p)} = M\alpha\mu b\sqrt{\rho_0 + \Delta\rho(\varepsilon_p)} \\ &= \sigma^0_{d-d}(\rho_0) + \sigma^*_{d-d}(\Delta\rho(\varepsilon_p))\end{aligned} \tag{5}$$

with $\sigma^0_{d-d} = M\alpha\mu b\sqrt{\rho_o}$ and where M is the Taylor's factor, α is a dimensionless constant, μ is the shear modulus and b the magnitude of the Burgers vector. In this equation, ρ_0 is the initial dislocation density and $\Delta\rho(\varepsilon_p)$ is the net increase of ρ at ε_p. Based upon the definition of the plastic strain hardening $\theta_p = d\sigma/d\varepsilon_p$, it follows that θ_p is equal to $d\sigma_{d-d}/d\varepsilon_p$. Considering the total dislocation density

ρ as the micromechanical parameter of the model, it follows from Eq. (5) that the strain-hardening is controlled by the evolution of the ρ with the plastic strain, i.e., $d\rho/d\varepsilon_p$. The strain evolution of ρ results from dislocation storage processes in the microstructure due to their immobilization at obstacles and from dislocation annihilation mechanisms. In a tempered martensitic structure, there are high-angle as well as low-angle internal interfaces. In the following, we assume that the effective mean displacement distance L of a dislocation, (the effective averaged distance that the dislocation moves before it gets definitely stored in the microstructure) is mainly mediated by high-angle boundaries. The low-angle boundaries between laths of the same variant (<2°) and boundaries between variants whose misorientation is 4.13° (different sub-blocks) are not necessarily considered as impenetrable obstacles. Therefore, the mean free path of a dislocation may be regarded as the dimension of a sub-block containing few tempered laths. The typical dimensions of these features are of the order of 1 μm. Thus, this value was selected as the mean free path of the moving dislocations. Further we assume that, over the limited deformation range investigated (<7%), the effective mean displacement distance L of a dislocation is constant with deformation. Assuming the dislocation dynamic recovery is linear in ρ, the dislocation density evolution equation can be written [9]

$$\frac{d\rho}{d\varepsilon_p} = M\left(\frac{1}{bL} - a\rho\right), \tag{6}$$

where the first term in the bracket is related to the storage mechanisms and the second to the annihilation processes, the coefficient a is the annihilation parameter. Since it is believed that the characteristic spacing between the high-angle boundaries controls the dislocation effective mean displacement distance, the dislocation evolution equation should be used, as indicated in [9] rather than the original one given by Kocks [8] in which the mean displacement distance stems from the dislocation spacing only. By combining Eqs. (5) with (6) and using the definition of the strain hardening $\theta_p = d\sigma_{d-d}/d\varepsilon_p$, the strain hardening can be expressed as

$$\begin{aligned}\theta_p(\sigma_{d-d}) &= \frac{P_1}{\sigma_{d-d}} - P_2\sigma_{d-d} \\ &= \frac{P_1}{\sigma^0_{d-d} + \sigma^*_{d-d}} - P_2(\sigma^0_{d-d} + \sigma^*_{d-d}),\end{aligned} \tag{7}$$

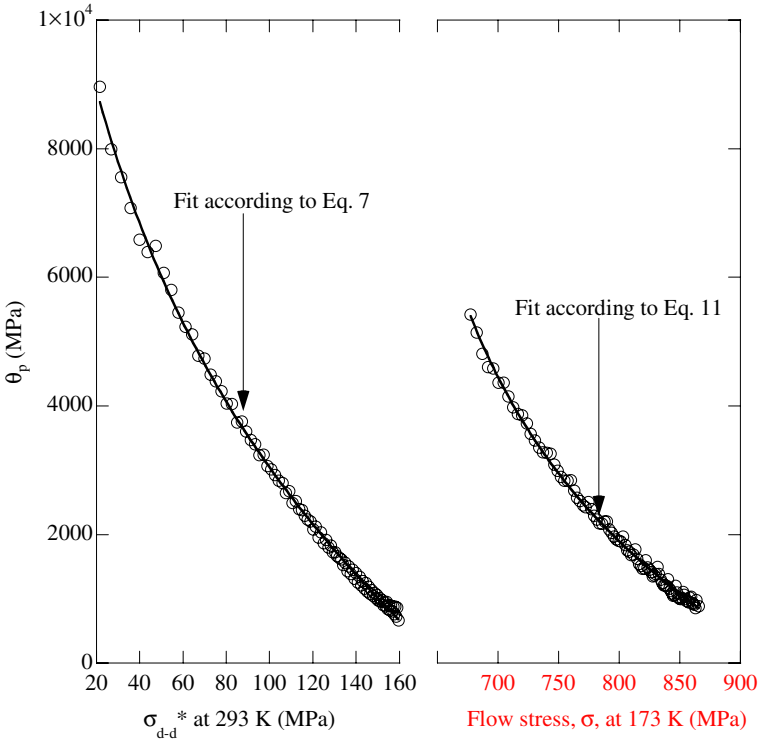

Fig. 3. $\theta_p(\sigma^*_{d-d})$ curve at 293 K and $\theta_p(\sigma)$ curve at 293 K Eurofer97.

with P_1 and P_2 are defined as: $P_1 = M^3(\alpha\mu)^2 b/2L$ and $P_2 = Ma/2$. Eq. (7) constitutes the strain-hardening law from room temperature and above. To check the validity of this law, we have calculated the strain-hardening from the experimental data and plotted it against the stress. As an example, θ_p versus σ^*_{d-d} at $T = 293$ K is presented in Fig. 3. Note in particular the curvature of the line, which is consistent with the stress dependence of the strain-hardening as predicted by Eq. (7). This fact is a direct consequence of the assumption of a constant mean free path with strain in the tempered martensitic microstructure.

Eq. (7) can be integrated to obtain $\sigma^*_{d-d}(\varepsilon_p)$, yielding:

$$\sigma^*_{d-d} = \sqrt{\frac{P_1 - (P_1 - P_2(\sigma^0_{d-d})^2)\exp(-2P_2(\varepsilon_p))}{P_2}} - \sigma^0_{d-d}. \tag{8}$$

Thus, the experimental stress–strain curve can be fitted using the last equation by adjusting P_1, P_2 and σ_0 parameters. This avoids calculating the strain-hardening rate. It is worth noting that Eq. (8) leads to a saturation stress σ_{sat} equal to $(P_1/P_2)^{0.5} - \sigma^0_{d-d}$.

Keeping in mind that three-parameter fits are used to reconstruct the deformation curves over a limited strain range, special attention has to be paid to the self-consistency of the analysis. We have to emphasize here that fitting the limited strain range of the experimental data with a three parameter equations is almost certain to properly reproduce the experimental data. Therefore, we constrained the fit by imposing a value to the mean free path of the dislocations once for all. As mentioned above the mean free path was considered equal to 1 μm. It is clear that the mean free path must remain essentially athermal and must have the same value over the temperature range over which the model holds. By doing so, only two parameters are left for fitting in Eqs. (7) or (8), which are P_2 and σ^0_{d-d}. In Table 1, we indicate the values of the coefficients that we use and that intervene in P_1, P_2 and σ^0_{d-d}. With these values and $L = 1$ μm, P_1 equals 0.93×10^6 MPa^2.

The temperature dependence of the two fitted parameters, P_2 and σ^0_{d-d}, are given in Fig. 4. Interest-

Table 1
Fixed coefficients used in Eq. (7)

M	α	G	b	L
3	0.2	80 000 MPa	0.268 nm	1 μm

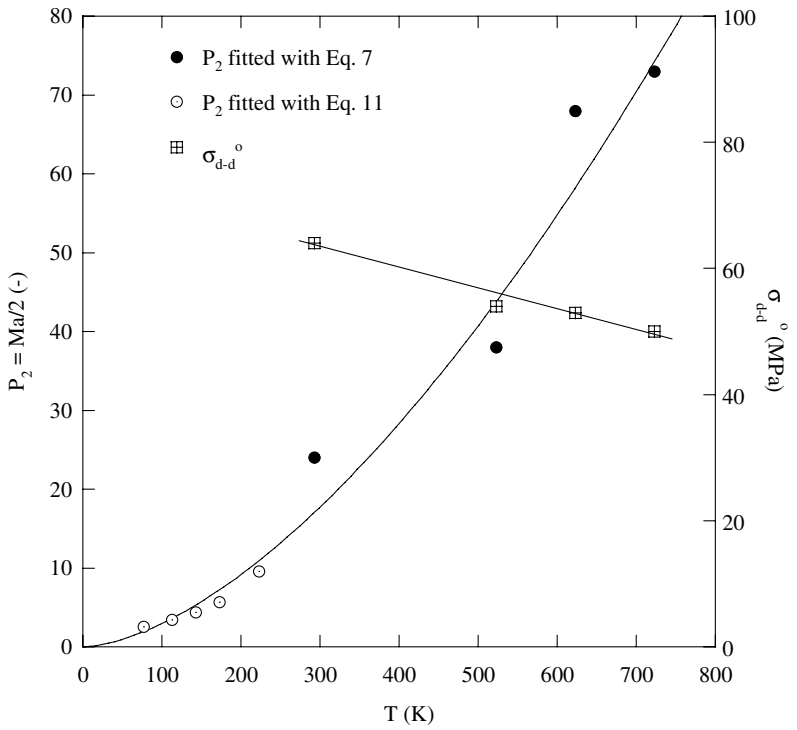

Fig. 4. Fitted P_2 and σ^0_{d-d} values versus temperature, Eurofer97.

ingly, the last plot reveals a significant temperature dependence of P_2. It increases with temperature, while only a very moderate one is found for σ^0_{d-d}. Such a behavior was actually expected since σ^0_{d-d} reflects the total dislocation density at the yield stress. This value should be mainly temperature independent even though small variations occur, associated with the temperature dependence of the shear modulus and with the amount of micro-plasticity taking place before macro-yielding. On the contrary, P_2, which is determined by all the dislocations annihilation processes, among which many are thermally activated, is expected to increase with temperature as observed. The value of σ^0_{d-d} is of the order of 55 MPa, which yields, with the use of Eq. (5), an initial dislocation density of about $1.8\times10^{13}\ m^{-2}$. Note that with the decomposition of the yield stress, Eq. (4), we believe that ρ_0 is representative of the dislocation density in the laths while the contribution of the dislocations in the boundaries is accounted for in $\tilde{\sigma}$ component. Using Eq. (4) at $\varepsilon_p = 0$, $\tilde{\sigma}$ is found to be equal to about 475 MPa. Finally, we note that the only parameter that remains ill-defined is the coefficient α of Taylor's equation (Eq. (5)). However, from the literature, it is known that α is of the order 0.1–0.5. We arbitrarily picked a value of 0.2.

3.3. Strain-hardening behavior below room temperature

For the BCC materials at $T < 0.2\ T_m$, the usual relationship between the flow stress and the square root of the dislocation density has been shown to be no longer valid [11]. Actually, the origin of this change has to be sought in the micro-mechanisms controlling the motion of dislocations. It is well established that the mobility of the dislocation screw segments in BCC metals is strongly reduced at low temperatures owing to the non-planar character of the dislocation core resulting in a strong lattice friction. Consequently, screw dislocations tend to arrange themselves in straight screw segments aligned along the $\langle 1\,1\,1\rangle$ directions under the presence of a stress field. The movement of these segments occurs by a thermally-activated mechanism of kink-pair formation followed by a fast movement of the kinks along the dislocation line. For BCC materials at low temperatures, Rauch [12] has presented a simple model, based upon energy balance considerations, where a new relationship between the applied stress and the dislocation density is proposed. In this model, the motion of the moving screw segments is analyzed in terms of a concomitant lattice friction and interaction with the forest dislocations. In the Appendix A the derivation of the new expression between the applied stress and the dislocation density is made. This relationship reads

$$\sigma = \frac{\sigma^* + 2\tilde{\sigma}}{2} + \frac{1}{2}\sqrt{(\sigma^*)^2 + 4(M\alpha\mu b)^2\rho(\varepsilon_p)}, \tag{9}$$

where σ^* is the effective stress required for double-kink nucleation at the imposed strain rate. σ^* strongly increases with decreasing temperature, and in the framework of the model it is considered to be independent of the actual state of the structure (dislocation density), i.e., $\sigma^* = \sigma^*(T)$. This expression appears as a more general equation than Eq. (5), which is actually obtained by setting $\sigma^* = 0$ in Eq. (9).

In order to write a plastic strain-hardening expression, we use the same strain dependence of the dislocation density as that in the case of high temperature, i.e., we use the Eq. (6). Then, Eq. (9) can be differentiated with respect to the plastic strain (ε_p) to obtain an expression for the plastic strain hardening

$$\frac{d\sigma}{d\varepsilon_p} = \frac{(M\alpha\mu b)^2}{((\sigma^*)^2 + 4(M\alpha\mu b)^2\rho)^{1/2}}\frac{d\rho}{d\varepsilon_p}. \tag{10}$$

Combining Eqs. (10) and (6), we obtain

$$\theta_p = \frac{M}{bL}\frac{(M\alpha\mu b)^2}{2\left(\sigma - \left(\frac{\sigma^*+2\tilde{\sigma}}{2}\right)\right)} + \frac{Ma(\sigma^*)^2}{8\left(\sigma - \left(\frac{\sigma^*+2\tilde{\sigma}}{2}\right)\right)} - \frac{Ma}{4}\left[2\left(\sigma - \left(\frac{\sigma^* + 2\tilde{\sigma}}{2}\right)\right)\right]. \tag{11}$$

Eq. (11) describes the plastic strain hardening evolution at constant plastic strain-rate and temperature in the Peierls regime. Let us compare Eq. (7) (or Eq. (8)) at high temperature with Eq. (11) at low temperature. In the first case (Eq. (7)), there are three constants to fit, namely the mean free path L, the annihilation coefficient a and σ^0_{d-d}. Eq. (11) has four parameters: L, a, $\tilde{\sigma}$ and σ^*. However, $\tilde{\sigma}$ can be estimated from the high temperature fits of Eq. (7), at room temperature. At this last temperature σ^0_{d-d} was about 55 MPa, using the Eq. (4) at $\varepsilon_p = 0$, a value of 475 MPa for $\tilde{\sigma}$ is found. Thus, we use this last value in Eq. (11) to fit the lower temperature $\theta_p(\sigma)$ curves, with $L = 1\ \mu m$ (dislocation mean free path) as it was for the high temperature case, and we fitted only σ^* and a. It was found that

the temperature dependence of σ^* reproduced fairly that of $\sigma_{0.2}$ and that the annihilation coefficient temperature dependence is consistent with that determined at high temperatures. This can be seen in Fig. 4 where we plot P_2 ($P_2 = Ma/2$) versus temperature. An example of low temperature fit is also given in Fig. 3.

4. Comparison of the fracture properties of the Eurofer97 steel with those of the F82H steel in the low transition

A new fracture toughness data set of Eurofer97 obtained with 0.35T $C(T)$ specimens has been reported by Bonadé et al. [13]. Hereafter, the data are analyzed within the framework of statistical models of cleavage, where the cumulative failure probability is given by [14]

$$P(K \leqslant K_{\mathrm{Jc}}) = 1 - \exp\left(\left(\frac{K - K_{\min}}{K_0 - K_{\min}}\right)^4\right). \tag{12}$$

The models predict the following statistical size effect on the measured fracture toughness, associated with the crack front length B:

$$K_{B_2} = K_{\min} + [K_{B_1} - K_{\min}] \cdot \left(\frac{B_1}{B_2}\right)^{1/4}. \tag{13}$$

For structural steels, it was found that the median fracture toughness–temperature curve of 1T thick specimen is well described by an equation of the type [1]:

$$K_{\mathrm{Jc\_median(1T)}} = a + b\exp(c(T - T_0)). \tag{14}$$

The previous equation is usually referred as to the master curve that can be indexed on an absolute temperature scale by T_0 at a reference toughness of 100 MPa $m^{1/2}$. The ASTM E1921-03 standard gives $a = 30$, $b = 70$ and $c = 0.019$ for 'ferritic' steels.

The testing of the Eurofer97 0.35T $C(T)$ specimens was performed between 125 K and 173 K where the measured fracture toughness remains below 150 MPa $m^{1/2}$ to avoid excessive constraint loss. The degree of in-plane constraint loss is usually characterized by the non-dimensional parameter $M = b\sigma_{0.2}E'/K^2$ where b is the ligament length, $\sigma_{0.2}$ the yield stress and E' the plane strain elastic modulus. The M values were all larger than 70. There-

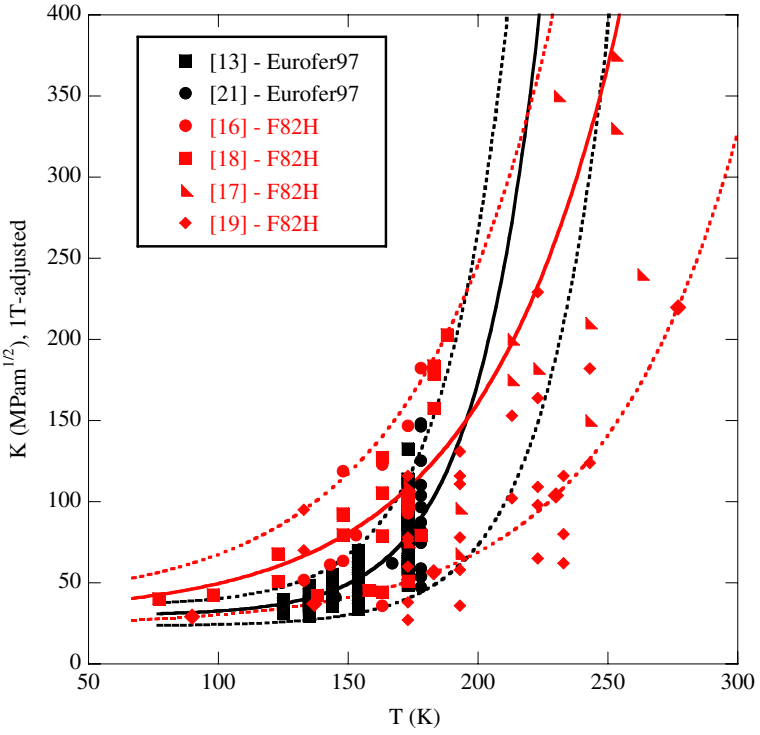

Fig. 5. 1T-adjusted data $C(T)$ data versus temperature of F82H and Eurofer97 with their corresponding master curve, 1% and 99% bounds (see text).

fore, it was assumed that, with such a M value, the constraint loss effect remains quite limited and the data were not constraint loss corrected. However, the data were adjusted to 1T size specimen according to Eq. (13). It was found that, in the temperature range investigated, the parameter c of the Eq. (14) had to be increased up to 0.04 to properly account for the temperature dependence of the median toughness (a and b was kept equal to 30 and 70 respectively). This result was actually unexpected because it was shown recently that the fracture toughness behavior of F82H steel is reasonably consistent with the ASTM E1921 master curve with $c = 0.019$ [15].

In Fig. 5 we compare the fracture behavior of Eurofer97 with that of F82H. The data for the F82H have been taken from the literature [16–19,21], from which we have included only the $C(T)$ data in the analysis that has been done following the ASTM E1921 procedure. All the data have been crack front length adjusted to 1T and the multi-temperature determination of T_0 has been applied. In Table 2, we summarize the reference temperature, the master curve shape we used as well as the temperature ranges over which the application of the two master curves were found to be satisfactory.

In Fig. 5, the 1% and 99% bounds of the cumulative probability to fracture are also plotted. As can be observed, the statistics underlying the master curve methodology describes well the scatter of both datasets with their respective master curve. For F82H, it has to be mentioned that some excessive scatter was found. More points than expected lie below the lower bound but all of them belong to the same dataset (from [19]), suggesting a lower toughness of this specific dataset, probably related to material variability. Finally, it is clear that additional testing of the Eurofer97 steel must be performed to better assess the master curve shape at higher temperatures and to understand the microstructural differences between the two steels that lead to the observed variation in the macroscopic fracture properties.

5. Fracture properties of the F82H steel after neutron irradiation

In this section, we present the fracture toughness data of F82H steel obtained with unirradiated as well as with irradiated $C(T)$ specimens according to the two irradiation conditions (SIWAS-09, SUMO-07) described in Section 2.3. The shift of the fracture toughness–temperature curve resulting from irradiation was determined using fracture data sets of $C(T)$ sub-sized specimens. 0.18T $C(T)$ were tested to characterize the fracture toughness properties of the unirradiated material as well as those after the two irradiations. However, five 0.35T $C(T)$ specimens from SIWAS-09 irradiation were also tested and analyzed along with twenty-three irradiated 0.18T $C(T)$ specimens. In this case, the testing was also focused on the low transition region, below an effective fracture toughness equal to 150 MPa $m^{1/2}$. For the unirradiated 0.18T $C(T)$ specimen at $T = 173$ K, the M value corresponding to 150 MPa $m^{1/2}$ (the highest) is of the order of 30. While constraint loss is expect to occur with such a value, the data reported hereafter have not been constraint corrected. As it was shown previously for F82H, the median fracture toughness–temperature curve of 1T-thick specimens is reasonably well described by the ASTM E1921 master curve. Thus, for the three sets of data (unirradiated, SIWAS-09, SUMO-07), the reference temperature T_0, at which the median toughness is 100 MPa $m^{1/2}$, was determined using the multi-temperature procedure as described in the ASTM standard E1921-03.

We recall that it is assumed that the shape of the master curve is not affected by irradiation. In Fig. 6, the 1T adjusted data of the unirradiated and irradiated after SIWAS-09 are plotted along with the master curve and associated 1% lower bound and 99% upper bound. The SUMO-07 data are not shown for the sake of clarity. The effect of the neutron irradiations at temperature below 673 K is to raise the yield stress by a given amount $\Delta\sigma_{0.2}$, which in turn induces a shift in ΔT_0. The conditions of SIWAS-09 and SUMO-07 irradiations belong to

Table 2
To with the respective MC equations for F82H and Eurofer97

Material	T_0 (K)	MC equations	T (K) range where the MC have been verified
F82H	167	$K_{med} = 30 + 70\exp(0.019(T - T_0))$	77–275
Eurofer97	179	$K_{med} = 30 + 70\exp(0.04(T - T_0))$	125–175

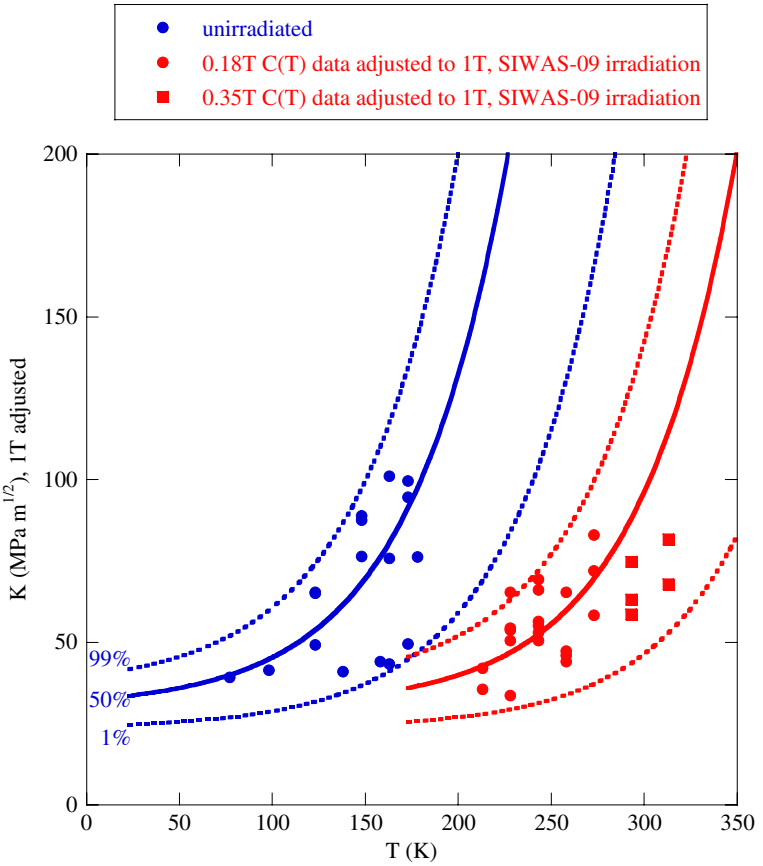

Fig. 6. 1T-adjusted fracture toughness data versus temperature. Unirradiated and irradiated F82H data, SIWAS-09 – 2.2 dpa at 333 K.

Table 3
To and To-shifts for SIWAS-09 and SUMO-07 irradiations, F82H

Condition	T_0 (K)	ΔT_0 (K)	Irradiation hardening $\Delta\sigma_{0.2}$ (MPa)
Unirradiated	180	–	–
SIWAS-09	303	123	300 ± 20
SUMO-07	328	148	300 ± 20

this so-called irradiation hardening regime. While the irradiation hardening has not been measured, a good estimate was done based upon similar irradiations performed in the HFR reactor (see Fig. 86 in [21]). In Table 3, we indicate these estimates of the irradiation hardening from which we derived the following relationship:

$$\Delta T_0 = (0.45 \pm 0.05)\Delta\sigma_{0.2}. \quad (15)$$

6. Conclusion

Tensile tests were performed to investigate the plastic flow properties of the Eurofer97 steel. Two temperature domains, below and above room temperature, were clearly identified in which the strain-hardening laws are different owing to the Peierls stress that acts on the screw dislocation segments at low temperature. Using values consistent with the tempered martensitic structure of the dislocation mean free path and dislocation density, the strain-hardening curves could be satisfactorily rationalized.

The fracture toughness properties of the Eurofer97 steel were investigated with 0.35T $C(T)$ specimens in the low transition and compared with those of the F82H steel. Over the temperature range, 125–175 K, we showed that the statistics of ASTM-E1921 master curve method does not provide a good description of the Eurofer97 scatter while it does for F82H.

The neutron-induced temperature shifts, ΔT_0, of the median fracture toughness temperature curve were determined for two irradiation conditions. It was established that ΔT_0 scales with the irradiation

hardening $\Delta\sigma_{0.2}$ according to $\Delta T_0/\Delta\sigma_{0.2} = 0.45 \pm 0.05$.

Acknowledgements

This work has been supported by the EFDA Technology Programme. The financial support of the Swiss National Foundation is gratefully acknowledged. The Paul Scherrer Institute is acknowledged for providing access to its facilities.

Appendix A

In the present work, we have used a similar approach as Rauch's formulation and applied it to the case of polycrystalline materials. In his original paper, Rauch decomposed the applied shear stress into the two components; one related to the thermal stress required to nucleate the double-kinks and one resulting from the interactions between the mobile and the forest dislocations. For the tempered martensitic steels, we considered an additional component for the flow stress, $\tilde{\sigma}$, which certainly cannot be neglected in case of a tempered martensitic alloy and which accounts at least for the high density of boundaries decorated by carbides. We also used the standard conversion between the applied stress, σ_a, and the shear stress τ_a, namely $\sigma_a = M\tau_a$, where M is the Taylor's.

Let us consider a screw dislocation moving at low temperature (Peierls regime) and pinned by forest dislocations as indicated in Fig. 7. Such a description of the motion of the screw segment is well supported by the in situ TEM observations of Louchet and Kubin [20]. In this case the decomposition of the applied shear stress is given by:

$$\tau_a = \tilde{\tau} + \tau_{d\text{-}d} + \tau^*, \tag{A.1}$$

where τ^* represents the lattice friction Peierls stress that is strongly temperature dependent. The actual screw segment length, L, is linked to the pinning points by mixed segments whose radii of curvature are R. R depends on the effective stress acting on the dislocation, defined by the difference between the applied stress and the back stress $\tilde{\tau}$, through the equation

$$R = \frac{\mu b}{\tau_a - \tilde{\tau}}. \tag{A.2}$$

Rauch indicated that, for this specific configuration of a moving screw dislocation, $\sigma_{d\text{-}d}$ arises from the extra energy needed to increase temporarily the dislocation length due to the formation of the mixed segments in comparison to a pure screw segment of length L_0. He also showed that $\sigma_{d\text{-}d}$ simply reads

$$\tau_{d\text{-}d} = 2\cos\phi\frac{\mu b}{L_0}, \tag{A.3}$$

where ϕ is the breaking-away angle when the screw dislocation has moved by a critical distance x_c.

In order to derive an expression between the applied stress and the dislocation density, we follow the geometrical consideration, of Louchet et al. who showed that the product between L_0 and x_c is equal to

$$L_0 x_c = \frac{1}{\rho}. \tag{A.4}$$

We emphasize here that L_0, the averaged distance between pinning points, depends on T. In fact, it increases with decreasing temperature, while x_c increases with increasing temperature.

A geometrical relationship between x_c, R and ϕ can be readily obtained from Fig. 7:

$$x_c = R(1 - \sin\phi). \tag{A.5}$$

By combining, the Eqs. (A.2)–(A.5), it is straightforward to obtain

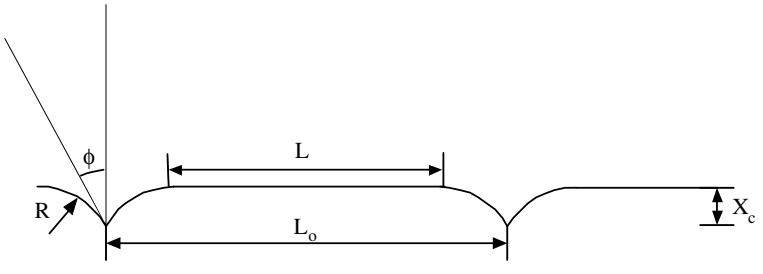

Fig. 7. Configuration of a moving screw dislocation at low temperatures.

$$\tau_{d-d} = 2\cos\phi\mu b\rho x_c = \frac{2\cos\phi(\mu b)^2\rho(1-\sin\phi)}{\tau_a - \tilde{\tau}}. \tag{A.6}$$

Finally, using the Taylor's factor M to convert the shear stress into the applied one, ($\sigma_a = M\tau_a$), the last equation can also be written as

$$\sigma = \frac{\sigma^* + 2\tilde{\sigma}}{2} + \frac{1}{2}\sqrt{(\sigma^*)^2 + 4(M\alpha\mu b)^2\rho} \tag{A.7}$$

with $\alpha^2 = 2\cos\phi(1-\sin\phi)$.

References

[1] K. Wallin, Int. J. Pressure Vessels Piping 55 (1) (1993) 61.
[2] G.R. Odette, K. Edsinger, G.E. Lucas, E. Donahue, in: Small Specimen Test Techniques, ASTM STP 1329, vol. 3, American Society for Testing and Materials, 1998, p. 298.
[3] G.R. Odette, T. Yamamoto, H.J. Rathbun, M.L. Hribernik, J.W. Rensman, J. Nucl. Mater. 323 (2003) 313.
[4] S. Jitsukawa, M. Tamura, B. van der Schaaf, R.L. Klueh, A. Alamo, C. Petersen, M. Schirra, P. Spaetig, G.R. Odette, A.A. Tavassoli, K. Shiba, A. Kohyama, A. KImura, J. Nucl. Mater. 307–311 (2002) 179.
[5] K. Edsinger, PhD Thesis, University of California, Santa Barbara, 1995, p. 115.
[6] J.E. Dorn, S. Rajnak, Trans. AIEM 230 (1964) 1052.
[7] P. Spätig, G.R. Odette, G.E. Lucas, J. Nucl. Mater. 275 (1999) 324.
[8] U.F. Kocks, J. Eng. Mater. Tech. (ASM H) 98 (1976) 76.
[9] Y. Estrin, H. Mecking, Acta Metall. 32 (1984) 57.
[10] G.E. Dieter, Mechanical Metallurgy, McGraw-Hill Book Co., London, UK, 1988.
[11] A.S. Keh, S. Weissmann, in: G. Thomas, J. Washburn (Eds.), Electron Microscopy and Strength of Crystals, Interscience Publishers, New York, 1963, p. 231.
[12] E.F. Rauch, Key Eng. Mater. 97&98 (1994) 371.
[13] R. Bonadé, P. Spätig, N. Baluc, J. Nucl. Mater., these Proceedings, doi:10.1016/j.jnucmat.2007.03.031.
[14] K. Wallin, J. Phys. IV C7 (1993) 575.
[15] G.R. Odette, T. Yamamoto, H. Kishimoto, M. Sokolov, P. Spätig, W.J. Yang, J.W. Rensman, G.E. Lucas, J. Nucl. Mater. 329–333 (2004) 1243.
[16] J. Rensman, J. van Hoepen, J. Bakker, R. den Boef, F. van der Broek, E. van Essen, J. Nucl. Mater. (2002) 245–311.
[17] K. Wallin, A. Laukkanen, S. Tähtinen, in: M.A. Sokolov, J.D. Landes, G.E. Lucas (Eds.), Small Specimens Test Techniques, ASTM STP 1418, vol. 4, American Society of Testing and Materials, Philadelphia, 2002, p. 33.
[18] P. Spätig, E. Donahue, G.R. Odette, G.E. Lucas, M. Victoria, in: L.P. Kubin, J.L. Bassani, K. Cho, H. Gao, R.L.B. Selinger (Eds.), Material Research Society Symposium Proceedings – Multiscale Modeling of Materials, 2001, p. Z7.8.1.
[19] M.A. Sokolov, R.L. Klueh, G.R. Odette, K. Shiba, H. Tanigawa, in: Effects of Radiation on Materials: 21st International Symposium, ASTM International, 2004, p. 408.
[20] F. Louchet, L.P. Kubin, Philos. Mag. A 39 (4) (1979) 443.
[21] J. Rensman, NRG-Report 20023/05.68497/P, 2005.